Electrochimica Acta 435 (2022) 141375

Contents lists available at ScienceDirect

Electrochimica Acta

journal homepage: www.journals.elsevier.com/electrochimica-acta

Controlling the triple phase boundary on Na-O_2 battery cathodes with perfluorinated polymers

M. Enterría [a,*], A. Letona-Elizburu [a,b], L. Medinilla [a], M. Echeverría [a], N. Ortiz-Vitoriano [a,c,*]

[a] Basque Research and Technology Alliance (BRTA), Center for Cooperative Research on Alternative Energies (CIC energiGUNE), Alava Technology Park, Albert Einstein 48, 01510, Spain
[b] University of the Basque Country (UPV / EHU), Barrio Sarriena, s/n, 48940 Leioa, Spain
[c] Ikerbasque, Basque Foundation for Science, María Díaz de Haro 3, Bilbao 48013, Spain

A B S T R A C T

Sodium-oxygen batteries hold great promise for the transition to a non-fossil fuel economy due to their high theoretical energy density. One of the most important components of these devices is the air-cathode, where the electrons available at the solid electrode, the Na^+ ions present in the liquid electrolyte and oxygen gas react to form sodium oxides as discharge products. The kinetics of the discharge/charge reactions depend significantly on the boundary points between the solid-liquid-gas reaction phases, known as triple phase boundary (TPB). The density of TPB points (and therefore the battery efficiency) can be maximized by incorporating perfluorinated polymers on the cathode formulation. Thus, this type of polymers enhance oxygen transport properties which favour the diffusion of gaseous components in detriment to liquid electrolytes on solid electrodes. In this work, polytetrafluoroethylene (PTFE) and fluorinated ethylene propylene (FEP) polymers were added in different weight ratio to commercial graphene nanoplatelets (GNPs) cathodes. The critical physical properties affecting the formation of the TPB have been identified and correlated to sodium-oxygen battery performance. These key properties, which are crucial to modulate the oxygen diffusion within the cathode structure, have been identified for the first time in this work for aprotic metal air devices. This approach is of outmost importance for the development or efficient electrochemical storage devices where oxygen gas is involved.

1. Introduction

The depletion of fossil fuels, the rapid evolution of the global economy and high living standards require the development of new energy storage systems that can support the needs of the world's population. During the last decade, aprotic sodium-oxygen batteries (Na-O_2) upsurged as a promising alternative to resolve future energy demands and environmental issues, due to their much higher theoretical energy density (1086 Wh kg^{-1} based on NaO_2 discharge product). Such energy density arises from a conversion-type mechanism where the electrochemical reduction/oxidation of molecular oxygen takes place to form different sodium oxides on the surface of the battery cathode (NaO_2, $Na_2O_2.2H_2O$, Na_2O…) [1]. The Na metal anode is oxidized and ions migrate to the cathode through a conductive organic electrolyte, whereas molecular oxygen is reduced (Oxygen Reduction Reaction, ORR) to superoxide (O_2^-) or peroxide (O_2^{2-}) radical/anions at the cathode. These oxygen reactive species generated during the ORR, combine with the metal cation and different metal oxides are formed at the surface or within of the "air-cathode" during discharge. Upon charging, the metal oxides are redissolved to perform the oxidation of the oxygen anions (Oxygen Evolution Reaction, OER) and subsequent deposition of the metal at the anode. ORR and OER are three-phase reactions comprising a gas (oxygen), a liquid electrolyte (Na^+ ions) and a solid cathode (electrons). The physical region where these three phases meet is commonly referred as the triple phase boundary (TPB, Scheme 1).

The density of TPB points is directly correlated with power and energy densities of the battery, where the interaction between the O_2 saturated electrolyte and active surface area of the cathode will dictate the kinetics of the discharge/charge reactions (ORR and OER) [2]. Because of the much larger oxygen diffusion coefficient in gas than in liquid phase [3,4], electrodes with mixed wettability (i.e., having regions with different electrolyte wettability coexisting in the same electrode section) could create phase boundaries that facilitate the oxygen transport through nonwetted pores. However, too many nonwetted pores will decrease the ionic conductivity of the electrodes as the liquid electrolyte is the phase providing the Na^+ ions [5]. Perfluoropolymers are largely used to bind the different components, enhance the mechanical strength and improve the adhesion of battery electrodes. This type of polymers offer a great opportunity to manufacture mixed-wettability cathodes as they are (i) excellent oxygen carriers, (ii)

* Corresponding authors at: Basque Research and Technology Alliance (BRTA), Center for Cooperative Research on Alternative Energies (CIC energiGUNE), Alava Technology Park, Albert Einstein 48, 01510, Spain.
E-mail addresses: menterria@cicenergigune.com (M. Enterría), nortiz@cicenergigune.com (N. Ortiz-Vitoriano).

https://doi.org/10.1016/j.electacta.2022.141375
Received 30 August 2022; Received in revised form 11 October 2022; Accepted 15 October 2022
Available online 19 October 2022

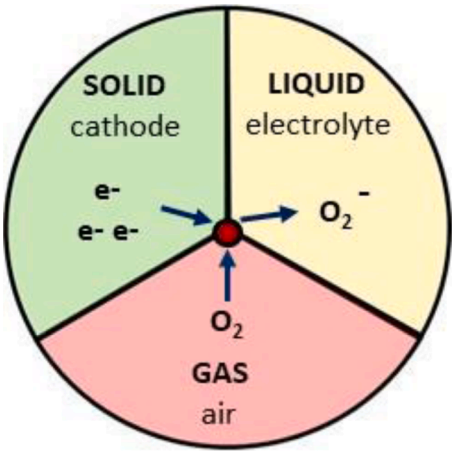

Scheme 1. Schematic representation of the triple phase boundary (TPB) in metal-air batteries.

not miscible/wettable in any solvent [6] and (iii) stable towards the attack of reactive superoxide radicals generated during discharge [5, 7–10]. In fact, perfluorinated compounds have been used in the biomedical field as artificial oxygen carriers in blood due to their ability to solubilize molecular O_2 [11–13]. However, the specific effect of these polymers on the oxygen transport in battery cathodes has been largely overlooked in literature. Here, we hypothesize that the use of certain amount of perfluoropolymers in the cathode formulation will enhance the O_2 transport while repealing organic electrolytes, therefore ensuring the coexistence of gas and liquid phases in the pore network of the cathode (i.e., reincreasing the number of TPB sites). Regarding the active material, carbon materials are extensively used as bifunctional catalysts in Na-O_2 battery cathodes due to their low cost, high surface area, chemical stability, conductivity, and intrinsic catalytic activity towards the ORR/OER reactions [14–18]. Their limited performance at high operating current densities boosted the research on new forms of carbon materials, where the open 2D structure of graphene offers an enhanced molecular diffusion in high-rate regime [19–26]. However, the processing of low-density graphene materials is very challenging and hinders its straightforward application in battery systems. Graphene nanosheets or nanoplatelets (GNPs) provide much better processability than few-layer graphene materials while deliver good electrochemical performance [27,28]. The effect of two perfluorinated polymers yielding different oxygen diffusion coefficients; polytetrafluoroethylene (PTFE, 10^{-6} cm^2 sec^{-1}) [29] and fluorinated ethylene propylene (FEP, 10^7 cm^2 sec^{-1}) [30], on the TPB formation of commercial GNP air-cathodes has been studied in this work. The electrolyte wettability, oxygen diffusion and electronic conductivity as function of the type of polymer and the weight ratio on cathode formulation has been studied by different characterization techniques, to establish a clear correlation between the cathode properties and their electrochemical performance.

2. Experimental

2.1. Electrode preparation

The electrodes were prepared by mixing a suitable amount of GNPs (xGnPs grade C–300, Sigma–Aldrich) and polytetrafluoroethylene (PTFE, 60 wt.% dispersion in H_2O Sigma–Aldrich) or fluorinated ethylene propylene (FEP, 55 wt.% dispersion in H_2O Fuel Cell Store) to obtain different active material to polymer binder mass ratios. Then, 3 mL of ethanol was added and the mixture was sonicated for 15 min to obtain a homogeneous dispersion, which was dried in air. The thus formed solid paste was kneaded until the formation of a homogeneous slurry and was punched out to obtain disc–shaped electrodes of 11 cm in diameter and 0.95 cm^2 in area. The electrodes were further dried at 250 °C under vacuum for 24 h and transferred to an Ar–filled glove box (H_2O < 0.1 ppm, O_2 < 0.1 ppm, Jacomex, France) without exposure to air. The mass and the thickness of the dry electrodes were in the range of 15–20 mg and 150–200 μm, respectively. A series of electrodes were prepared by using PTFE as binder and named as X_PTFE where X is the weight percentage of PTFE (series 1, Table 1). Unlike PTFE, it was not possible to bind the GNP powder by using only FEP polymer. The addition of a small amount of PTFE in the electrode formulation (5 wt. %) enabled processable pastes. Therefore, a second series of electrodes were prepared by fixing the amount of PTFE while varying the proportion of FEP. The electrodes were named as X/Y_FEP/PTFE where X and Y are the weight percentage of PTFE and FEP polymer, respectively (series 2, Table 1).

2.2. Sodium-air cell assembly

The modified Swagelok®-type cells assembled in this work consisted of a sodium metal anode (10 mm, Panreac), a sodium conducting electrolyte and the GNP cathodes shown in Table 1. Prior to the assembly, the cells were dried overnight at 60 °C in vacuum and transferred to an Argon filled glovebox (H_2O < 0.1 ppm, O_2 < 0.1 ppm, Jacomex). The self-standing graphene cathodes were dried overnight at 200 °C in vacuum, transferred to the glove box and supported on a 12 mm diameter stainless steel mesh (Alfa Aesar) current collector. Three Celgard® H2010 papers (13 mm) were soaked in 200 μL of electrolyte and used as separators. Ethylene glycol dimethyl ether solvent (DME, anhydrous, 99.5% Sigma Aldrich) and sodium trifluoromethanesulfonate salt (NaOTf, 99.5%, Solvionic) were used to prepare the 0.5 M NaOTf in DME electrolyte. To this end, DME was dried over molecular sieves (3 Å, Sigma Aldrich) for one week and NaOTf salt under vacuum at 110 °C for 48 h. The water content in the prepared electrolytes was measured with an 899 Karl Fisher Coulometer (Metrohm) and was below 10 ppm in all the cases. Following the assembly, Na-O_2 cells were pressurized with pure oxygen (99.99% pure) to ~ 1 atm and rested for 8 h at open circuit voltage ≈ 2.2–2.3 V (vs Na^+/Na) before the electrochemical measurements. Galvanostatic deep-discharge experiments were performed using a Biologic-SAS VMP3 potentiostat at a current density of 0.2 mA cm^{-2} and a voltage cut off of 1.8 V (vs Na^+/Na). Shallow cycling measurements were performed by galvanostatic charge-discharge in the same conditions, within a potential range of 1.8–3.2 V (vs Na^+/Na) and a capacity cut-off of 0.5 mA cm^{-2}.

2.3. Physicochemical characterization of pristine materials and discharged electrodes

The porosity of the pristine GNPs was analysed by nitrogen gas physisorption using an ASAP2460 adsorption analyser (Micromeritics) to measure the N_2 adsorption–desorption isotherms at –196 °C in the relative pressure range from 10^{-4} to 0.99. Samples were degassed at 200 °C for 16 h under vacuum. The specific surface area (S_{BET}) was calculated according to the Brunauer-Emmett-Teller (BET) method [31] from the nitrogen isotherms in the relative pressure range of 0.05–0.25. The total volume of micro–mesopores (V_T) was calculated as the amount

Table 1
Summary of the materials along with the acronyms used in this work.

		wt.% in electrode formulation			
	Electrode name	GNPs	PTFE	FEP	Total amount of binder
series 1	**5_PTFE**	95	5	0	5
	10_PTFE	90	10	0	10
	15_PTFE	85	15	0	15
	20_PTFE	80	20	0	20
series 2	**5/5_FEP/PTFE**	90	5	5	10
	10/5_FEP/PTFE	85	5	10	15
	15/5_FEP/PTFE	80	5	15	20

of N_2 adsorbed at a relative pressure of 0.99. The different crystalline phases present on the pristine GNPs, pristine cathodes or the discharged cathodes were studied by X-ray diffraction (XRD) using a Bruker D8 Discover diffractometer with θ/2θ Bragg–Brentano geometry (monochromatic Cu radiation: Kα1 = 1.54056 Å). The patterns were acquired within the 10–70° range (2θ) with a resolution of 0.02°/step and an accumulation time of 1.2 s/step. The morphology of either the cathodes or the electrochemical formed products on the discharged cathodes were evaluated by scanning electron microscopy (SEM) imaging using a FEI Quanta 250 microscope operating at 20 kV. The surface composition in both plain and cross-sectional view of the cathodes was studied by energy dispersive X-ray spectroscopy (EDX) using the same equipment with an ADC1 detector and a magnification of 750. The Raman spectra of the all the materials were recorded with a Renishaw spectrometer (Nanonics Multiview 2000) operating with an excitation wavelength of 532 nm, focused with a 50x long working distance objective. The spectra were obtained by performing 10 acquisitions with 10 s of exposure time of the laser beam to the sample. A silicon wafer was used for calibration. In the case of the discharged cathodes (sensitive samples) they were transferred from an Ar–filled glove box to the different equipment using air–tight holders to avoid air exposure.

2.5. Evaluation of the electronic conductivity, wettability and oxygen diffusion in GNP/polymer binder cathodes

Double-layer capacitance [32] is related to the wetted interfacial area on an electrode via the following equation.

$$C = \varepsilon_r \varepsilon_0 \frac{A}{d} \quad (1)$$

where C is the capacitance, ε_r is the relative permittivity of the electrolyte, ε_0 is the permittivity of the vacuum, d is the double layer thickness and A represents the wetted pore surface. As ε_r, ε_0 and d can be considered constant for a given electrolyte the change of the area of the wetted pore surface is proportional to the variation of the double-layer capacitance. Hence, the wetting ability of a solid by an electrolyte can be quantified by cyclic voltammetry (CV), through integration of the area inside the current-potential curve. For this purpose, it is necessary to consider that the capacitor consists of two electrodes connected in series and use the following equation:

$$C = \frac{2C_{cell}}{m_{electr}} = \frac{2C_{cell}}{\frac{m}{2}} = 4 \cdot \frac{I \cdot \frac{dt}{dV}}{m} = 4 \cdot \frac{I}{m \cdot s} \quad (2)$$

where C is the capacitance, C_{cell} is the cell capacitance, m_{electr} the electrode mass, m the mass of the active material, s (dt/dV) the scan rate and I is the current. The wettability can be also studied by electrochemical impedance spectroscopy (EIS), where ideally polarizable (wettable) electrodes would display a straight line parallel to the imaginary axis at low frequencies in the Nyquist plot (negative imaginary impedance vs the real part of the impedance). A symmetric Swagelok® type cell was assembled using two GNP/polymer binder electrodes, with similar weights and thicknesses. CV cycles were performed at a sweep rate of 10 mV/s in a voltage window from 0 to 1.4 V while EIS scans were conducted from 100,000 kHz to 10,000 mHz. Three cells were assembled for each experiment to ensure reproducibility and get the standard deviation value. Prior to the measurements, the electrodes were soaked in 200 μL of 0.5 M NaOTf in DME and separated by two Celgard® H2010 separators (13 mm diameter). The cell and the GNP electrodes were dried overnight at 60 °C and 200 °C in vacuum, respectively; and transferred to the Argon-filled glovebox prior to the assembly. The electronic conductivity measurements were performed in an Everbeing SR-4–6 L four-point prober by applying the Van der Pauw method. A constant current (9–10 mA) was applied through the two outer tungsten pins using a DC current source (Keithley 6220) while the corresponding voltage drop was measured across the two inner tungsten pins with a nanovoltmeter (Keithley 2182A) [33]. The measurements were conducted at 25 °C with and an environmental moisture of 66%. Each electrode was measured six times in different parts of the electrode and the standard deviation was calculated.

Oxygen diffusion within the cathode bulk was estimated by EDX imaging, studying the distribution of the discharge products throughout their cross-section. To that end, the discharged electrodes were carefully cut in half inside a globe box using a scalpel and transported to the SEM equipment in an air-tight holder. Cross-sectional EDX mapping images were acquired for C, F, O and Na atoms at a magnification of x850. The contribution of each of them was registered on an a Thermo Fisher Quanta 200 FEG high-resolution Scanning Electron Microscope (SEM), equipped with an ADC1 detector operating at 20.00 kV, spot size set at 4.5 and a dwell of 2000 us.

3. Results and discussion

3.1. Physicochemical characterization of GNPs and electrode pastes

The porosity of the GNPs was evaluated by N_2 adsorption at –196 °C (Fig. 1a). The amount of adsorbed nitrogen at low relative pressures indicated the presence of micropores where the calculated BET surface area was 302 $m^2\ g^{-1}$. The incipient slope and the presence of a slight hysteresis loop at medium-high relative pressures revealed the moderate presence of mesopores. The total pore volume calculated at a P/P_0 of 0.99 was 0.55 $cm^3\ g^{-1}$. It can be therefore concluded that GNPs have a relatively high surface area with some mesopore contribution. The structure of the GNPs was studied by XRD and Raman spectroscopy. The XRD pattern (Fig. 1b) showed the three characteristics peaks of graphite at 26.45°, 42.31° and 54.45° corresponding to (002), (101) and (004) reflections, respectively. Hence, GNPs seemed to present a multilayer structure characteristic of graphene with low exfoliation degree [34,35]. The Raman spectra of pristine GNPs also displayed peaks characteristic of graphitic materials (Fig. 1c):(1) the D band at 1340 cm^{-1}, which is associated with the disordered structure of the graphitic materials, representing the breathing vibration of sp^2-hybridized, aromatic carbon rings located next to an edge or defect in the lattice, (2) the G band at 1585 cm^{-1}, related to stretching vibration of sp^2-based C=C bonds and (3) the second-order Raman spectra (i.e., the 2300–3300 cm^{-1} region) where different low–intensity bands appear. Consistent with XRD, the larger intensity of the G band compared with the D band in Fig. 1c indicated a predominantly graphitic structure of the GNP material. As well, the noticeable intensity and the symmetric shape of the 2D band revealed a turbostatic structure where the graphene sheets are randomly stacked [36]. Commercial GNPs, therefore, presented a graphitic composition with randomly stacked graphene nanosheets that might make this material an excellent electrical conductor. The morphology of this commercial material was studied by SEM imaging (Fig. 1d) where small particles of 2–4 μm together with ~ 25 μm big aggregates were observed. The small particle size, the platelet morphology, and the micro–mesoporous structure could provide this material with an open/accessible surface area to accommodate the deposition of the discharge products and enhance their dissolution during Na-O_2 battery cycling.

As explained in Section 2.1 the GNPs were processed by adding polyfluoropolymers (PTFE or/and FEP) as binders and/or plasticizers to achieve mechanically stable and handy electrode pastes (Fig. S1). The morphology of the prepared electrodes, as well as the dispersion of the F-containing polymer binder in them, was studied by cross-sectional SEM-EDX imaging (Fig. S2). A close inspection at high magnification (x10,000) revealed that both 5_PTFE and 10_PTFE presented a homogeneous particle distribution while 15_PTFE and 20_PTFE showed large particle aggregates and, consequently, inhomogeneous surface (Fig. S2a–d). The dispersion of the particles followed the same trend for PTFE/FEP series (Fig. S2e–g), worsening as the proportion of binder increases. The EDX analysis of the full cross sections (Fig. S2) revealed a

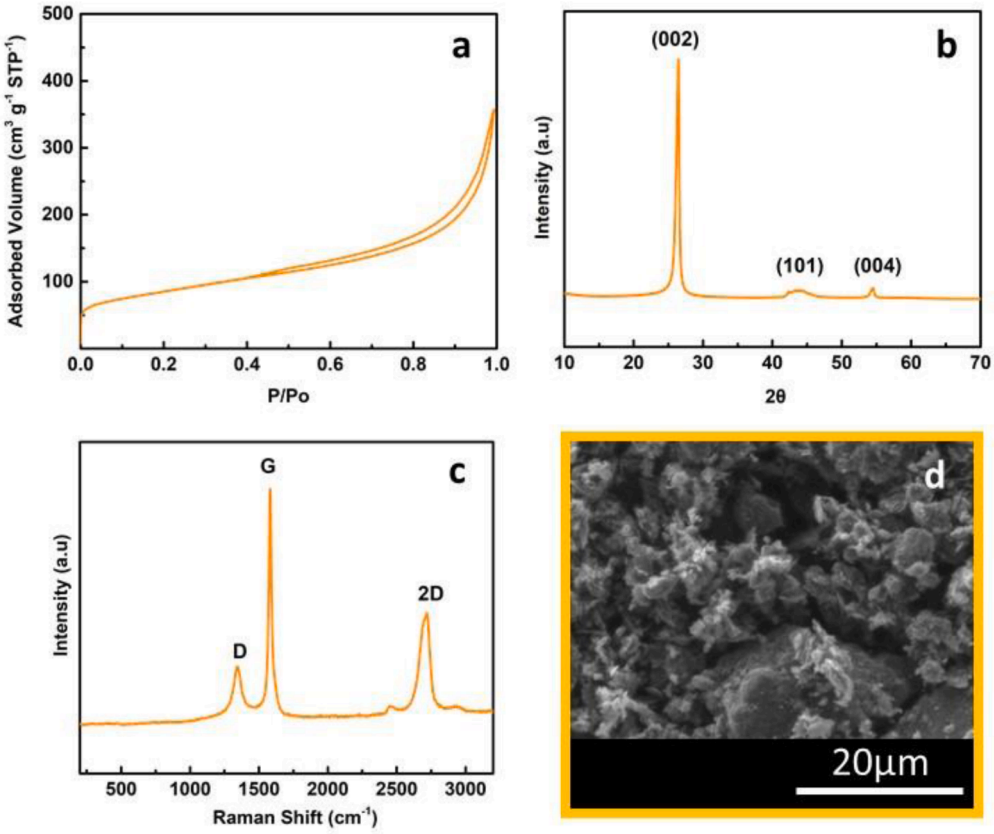

Fig. 1. (a) N_2 adsorption/desorption isotherm at –196 °C, (b) XRD pattern, (c) Raman spectra and (d) SEM image of pristine GNPs.

suitable distribution of the fluorine atom (i.e., the polymer binder) for the GNP/PTFE electrode series. However, it was slightly uneven for PTFE proportions above 10 wt.% and, particularly, for 20_PTFE sample. The dispersion of the binder was more deficient for PTFE/FEP series, where the agglomeration of F atoms along the electrode transversal section was visible, even at low polymer weight fractions (5/5_PTFE/FEP sample).

3.2. Characterization of the discharged cathodes

The ORR kinetics on GNP cathodes were examined upon galvanostatic discharge on a Na-O_2 full cell. Fig. 2 shows the voltage profiles for all the cathodes discharged to full capacity in 0.5 M NaOTf in DME electrolyte at a current density of 0.2 mA cm^{-2} and a voltage cut–off of 1.8 V. In the case of the cathodes processed only with PTFE, the largest capacity was reached for polymer proportions of 10 wt.% (10_PTFE) while decreased significantly for proportions above that value (15_PTFE and 20_PTFE). Thus, 10_PTFE and 5_PTFE cathodes presented larger discharge capacity (4.51 mAh cm^{-2} and 3.40 mAh cm^{-2}) than 15_PTFE (2.16 mAh cm^{-2}) and 20_PTFE (2.08 mAh cm^{-2}). Considering only the content of FEP polymer in FEP/PTFE series (Table 1), the obtained capacities were very similar to those in PTFE series (i.e., 10_PTFE = 10/5_FEP/PTFE > 5_PTFE=5/5_FEP/PTFE > 20_PTFE = 15/5_FEP/PTFE). However, if the total amount of polymer is considered (Table 1), the discharge capacity was maximized for polymer ratios around 15 wt.% (10/5_FEP/PTFE). It can be therefore concluded that the discharge capacity is greatly affected by the total weight of polymer rather than its nature, where the capacity is maximized for ratios from 10 to 15 wt.%.

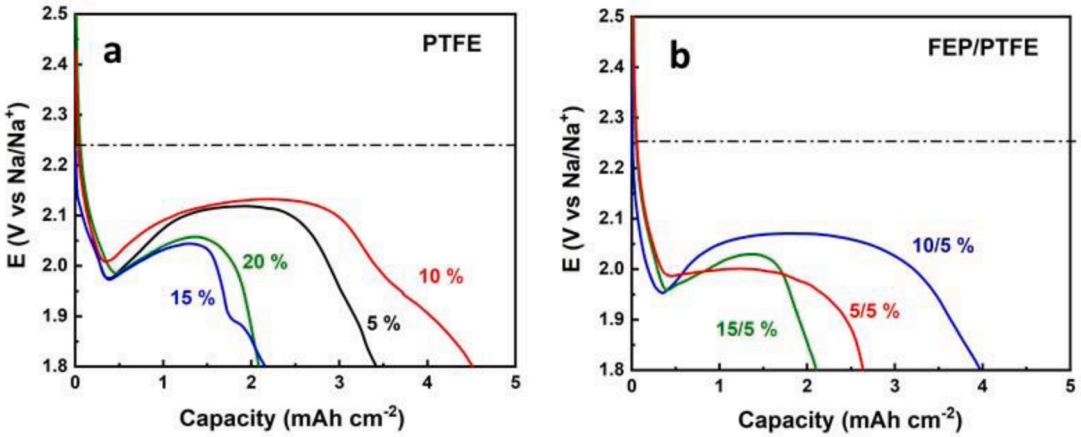

Fig. 2. Galvanostatic full discharge profiles on a Na-O_2 full cell in 0.5 M NaOTf in DME at 0.2 mA cm^{-2} of (a) GNP/PTFE and (b) GNP/FEP/PTFE cathodes.

The discharge overpotential is also an important parameter in the electrochemical performance of a given cathode. The overpotential, which is related with kinetical limitations, is the potential difference (voltage) between a reaction standard reduction potential and the potential at which the reaction is experimentally observed. The cathodes with a larger proportion of PTFE binder not only yielded more limited discharge capacities but also larger overpotentials. Hence, 10_PTFE and 5_PTFE presented a plateau at 2.12 V vs $E^0(Na/NaO_2) = 2.27$ V (150 mV overpotential) while the plateau in 15_PTFE and 20_PTFE was at 2.03 V (corresponding to a 240 mV overpotential). As well, the FEP/PTFE cathodes showed higher overpotential (200–240 mV) as compared with PTFE series, where 10/5_FEP/PTFE yielded the lowest overpotential.

The evolution of the morphology of the discharge products on the different cathodes was studied by SEM imaging in Fig. S3. All the cathodes presented cubic-like deposits on their surface and this morphology is generally associated to the formation of sodium superoxide (NaO_2) as discharge product. The particle size of the cubic-like discharge products decreases as the weight ratio of polymer in the cathode formulation increases. Hence, the particle size decreases from 20 μm in 5_PTFE sample to 10 μm in 20_PTFE cathode. The density of NaO_2 cubes increases substantially when increasing the PTFE ratios above 5 wt.%, where the maximum density is achieved for 10_PTFE sample. In the case of FEP/PTFE series, the particle size also decreases from 25 μm in 5/5_FEP/PTFE to 10 μm in 15/5_FEP/PTFE, but the density of cubic-like particles does not change much. The nature of the discharge products was further evaluated by Raman spectroscopy (Fig. 3). All the cathodes displayed the D, G and 2D bands arising from the graphitic structure of GNPs (Fig. 1c), whose Raman spectra is displayed at the bottom of Fig. 3a for comparison. The presence of an intense peak centred at 1156 cm^{-1} for all the discharged cathodes confirmed that NaO_2 is the main discharge product, regardless of the nature and the proportion of polymer binder. However, a close inspection of the 1000–1300 cm^{-1} region revealed a small peak at 1136 cm^{-1} in the spectra (Fig. 3b). This peak, which is related to the formation of hydrated sodium peroxide ($Na_2O_2{\cdot}2H_2O$), was more noticeable for the cathodes in FEP/PTFE series. In the case of PTFE series, those cathodes containing more than 10 wt.% of polymer yielded more intense $Na_2O_2{\cdot}2H_2O$ signal. (Fig. 3b). The presence of NaO_2 as main discharge product in all the studied cathodes (Fig. S4a, b) as well as the existence of $Na_2O_2{\cdot}2H_2O$ as minoritarian side product in some of them (Fig. S4c–i), was further confirmed by surface mapping in Fig. S4. The formation of $Na_2O_2{\cdot}2H_2O$ as parasitic product is generally observed in Na-O_2 batteries where the Na_2O_2 is readily hydrated by any moisture in electrolyte or the gas feeding [37–40]. The presence of NaO_2 was also observed by XRD characterization (Fig. S5a), where two intense peaks at $2\theta \approx 32.7^\circ$ and 46.8° corresponding to (200) and (220) diffraction planes in NaO_2 are verified for all the discharged cathodes. Interestingly, the peak ascribed to (004) diffraction plane in GNPs (Fig. 1b), was visible for all the samples in PTFE series, but it was not in the case of FEP/PTFE series (Fig. S4a). This suggests a better coating of GNP particles by FEP polymer as compared with PTFE or, a larger passivation of the electrode surface by the discharge products. To discern which of the two hypothesis is actually occurring, pristine 20_PTFE and 15/5_FEP/PTFE electrodes were studied by XRD. The peak associated to GNPs is visible for both patterns in Fig. S5b, confirming a larger passivation of the surface on FEP-containing cathodes.

The cycling performance of the GNP/PTFE cathodes was examined at a current density of 0.2 mA cm^{-2} by shallow–cycling experiments, where the depth of discharge was limited to 0.5 mAh cm^{-2} (Fig. 4). 10_PTFE cathode presented the largest cyclability by delivering 142 cycles, followed by 5_PTFE (123 cycles) and 15_PTFE (111 cycles). The lowest cycling performance was observed for 20_PTFE cathode which yielded 27 cycles (Fig. 4a). Even though, all the cathodes presented a good coulombic efficiency in the first cycles, 10_PTFE reached 100% efficiency after only 20 cycles. This was not the case for 5_PTFE and 15_PTFE, where full recovery of the efficiency was delayed to 40 and 80 cycles, respectively. 20_PTFE not only presented poor cycle life but also deficient efficiency throughout the entire cycling. The cycling performance of FEP/PTFE cathodes was much lower than that in PTFE series; none of them exceeded 37 cycles regardless of the total polymer proportion (Fig. 4b). 5/5 FEP/PTFE cathode showed the best cycling performance (37 cycles) and the best coulombic efficiency (100% above 10 cycles) of its series. In contrast, 10/5 FEP/PTFE (16 cycles) and 15/5 FEP/PTFE (31 cycles) presented poor cyclability and the latter also displayed a very low coulombic efficiency. The evolution of the cell overpotential with the number of cycles is shown in Fig. 4c for all the studied cathodes. Generally, a gradual increase of the overpotential was observed over cycling, probably due to the accumulation of insoluble discharge products and pore clogging. This fact is characteristic of Na-O_2 batteries, due to the formation of an electrical insulating passivation layer of discharge product that saturates active sites in the cathode [41, 42]. Except 20_PTFE (> 850 mV), the cathodes presenting the lowest overpotentials were those containing PTFE binder (< 350 mV up to 60 cycles). In the case of FEP/PTFE series, not only the overpotential was much higher (> 500 mV) but also increased drastically with the total proportion of binder. In contrast, the increment on the overpotential was almost negligible when the proportion of PTFE was increased from 5_PTFE to 15_PTFE cathodes. However, further increase of PTFE proportion up to 20 wt.% causes a twofold increase on the overpotential, where 20_PTFE sample presented values similar to FEP/PTFE series.

The state-of-art on best-performing carbon-based Na-O_2 battery cathodes [25,41,42], taking into account comparable electrode mass

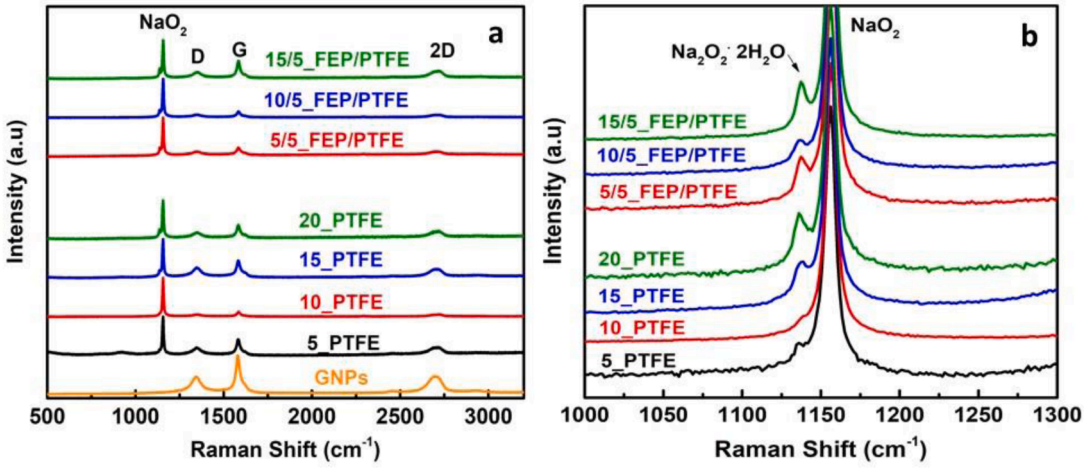

Fig. 3. (a) Raman spectra and (b) zoom of the 1100–1300 cm^{-1} region for all the discharged cathodes.

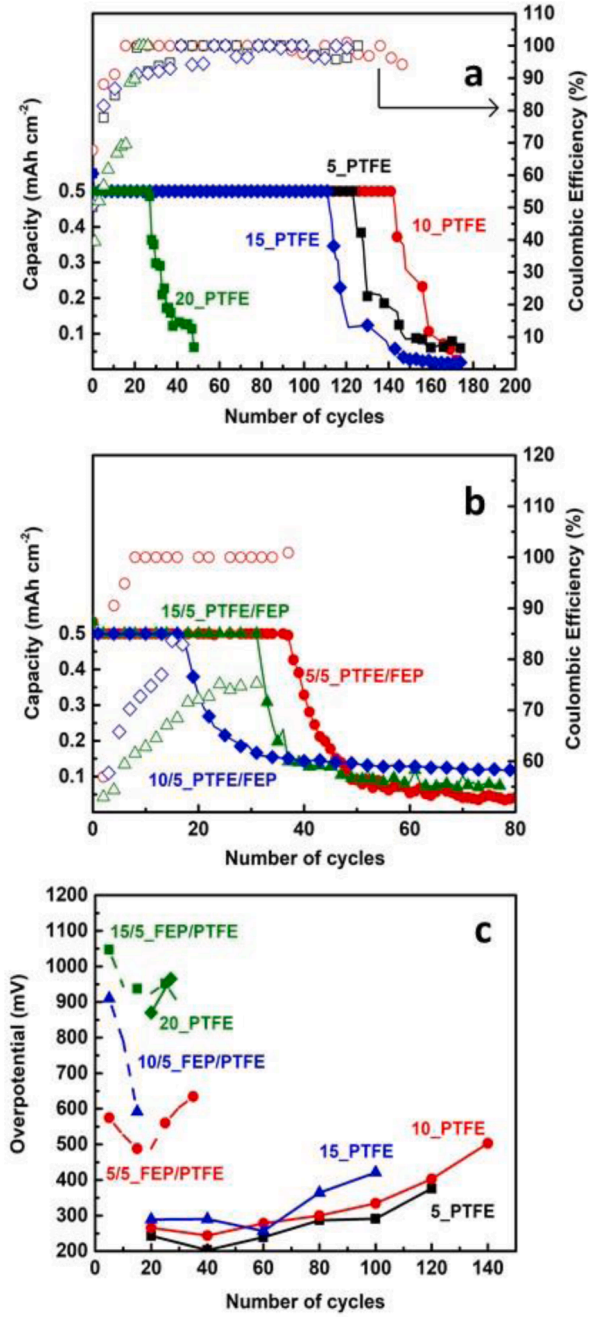

Fig. 4. Evolution of the discharge capacity (left axis, points denoted as filled symbols) and coulombic efficiency (right axis, points denoted as open symbols) with the number of cycles for (a) PTFE and (b) FEP/PTFE series. (c) Overpotential evolution with the number of cycles for all studied electrodes, at a current density of 0.2 mA cm^{-2}.

loading, current density and capacity cut off to the present work, revealed that the performance of 10_PTFE cathode exceeded those in literature. Thus, ruthenium/carbon nanotubes composites yielded 110 cycles at 0.19 mA cm^{-2} to 0.4 mAh cm^{-2} but showing a high cycling overpotential of 1.1 V [43]. $La_2Co_2O_7$/activated carbon composites delivered 167 cycles with 0.4 V overpotential at 0.09 mA cm^{-2} to 0.9 mAh cm^{-2} [44]. 3D printed reduced graphene oxide [20] or nucleotide/graphene hybrids [41] delivered a remarkable cycle life of 120 cycles (at 0.34 mA cm^{-2} to 0.34 mAh cm^{-2}) and 95 cycles (at 0.2 mA cm^{-2} to 0.5 mAh cm^{-2}) respectively, both with 0.4 V of overpotential. Polypirrole-based nitrogen-doped carbon nanofiber released a cycling performance of 90 cycles at 0.5 V overpotential, but with quite low operating current density (0.07 mA cm^{-2}) [45]. Finally, multidoped carbon fibres presented an excellent long-term cycling, comparable with that in 10_PTFE electrode, by delivering 157 cycles at high current density (0.6 mA cm^{-2}) to 0.35 mAh cm^{-2} in polyionic liquid electrolyte [46].

3.3. Electronic conductivity, wettability and oxygen diffusion in GNP/polymer binder cathodes

To further understand the electrochemical performance of the GNP/polymer binder cathodes, the three physical properties which play a key role in the formation of the triple phase boundary were studied: the electronic conductivity, the electrolyte wettability and the oxygen transport. The electronic conductivity decreased substantially from 5_PTFE (631 S m^{-1}) to 10_PTFE (500 S m^{-1}) for further remaining constant for polymer proportions up to 15 wt.% (Fig. 5a). The use of larger polymer weight ratios in 20_PTFE caused a noticeable decrease on the electronic conductivity until 290 S m^{-1}. Although the values were slightly lower (349–477 S m^{-1}), the evolution of the electronic conductivity showed the same behavior in the FEP-containing cathodes. The wettability of the different cathodes in 0.5 M NaOTf in DME electrolyte was studied by integration of the respective cyclic voltammetry curve (Section 2.4, Fig. 5b). The wettability of the GNP-based cathodes remained more or less constant when adding PTFE or FEP ratios below 15 wt.%. The addition of larger amounts of binder in 20_PTFE or 15/5_FEP/PTFE electrodes led to a noticeable decrease on the wettability, where it was much pronounced in the cathodes containing FEP polymer. The evolution of the capacitance on the Nyquist plots (Fig. 5c) was quite consistent with that in CV measurements. The slope of the EIS curve at low frequencies decreased from 5_PTFE to 20_PTFE, indicating a gradual decrease on the electrode wettability as the polymer weight ratio increased. 5_PTFE showed the highest wettability with the steeper slope while 10_PTFE and 15_PTFE cathodes presented an intermediate slope. In the case of FEP/PTFE series, the slope decreased from 5/5_FEP/PTFE to 15/5_FEP/PTFE but presented a sudden increase for 10/5_FEP/PTFE cathode. A combined analysis of CV (Fig. 5b) and EIS measurements (Fig. 5c) suggest that there is a sudden increase of wettability for the cathodes containing ~ 15 wt.% of perfluorinated polymer binder, either 10_PTFE or 10/5 FEP/PTFE. This could be ascribed to an inhomogeneous dispersion of PTFE or FEP on those cathodes containing weight ratios above 10 wt.% (Fig. S2). Hence, the electrolyte may flow withing the non-coated GNPs, which will present more affinity towards the electrolyte compared with the domains rich in polymer binder. This did no happened for 20_PTFE and 10/5_FEP/PTFE as at such large proportions the wettability of the cathodes is very low (Fig. 5b), regardless of the polymer dispersion. It can be concluded that i) PTFE yields slightly better electron conduction and electrolyte wettability than FEP/PTFE mixture and ii) both properties deteriorate significantly for polymer weight ratios above 15 wt.%.

The diffusion of both the electrolyte and oxygen gas along the cathode bulk was studied by SEM/EDX imaging. To this aim, the cathodes discharged in Fig. 2 were cut in half and the distribution of the solid discharge products along the cross-sectional area was monitored in Fig. 6. The top part of the electrodes in the images corresponds to the oxygen/cathode interface while the bottom part corresponds to the cathode/electrolyte interface. The formation of NaO_2 (green and yellow deposits in Fig. 6) in 5_PTFE is distributed throughout the transversal area of the cathode (Fig. 6a). This indicates that both the electrolyte and the O_2 were able to flow smoothly from the opposite interfaces to form the discharge products. However, the micron-sized sodium oxide deposits were progressively displaced towards the cathode/electrolyte interface (i.e., bottom part in the images) when increasing the PTFE proportion from 10_PTFE (Fig. 6b) to 20_PTFE (Fig. 6d). Such displacement may be caused by a preferential diffusion of oxygen over the liquid electrolyte through the cathode bulk, caused by an

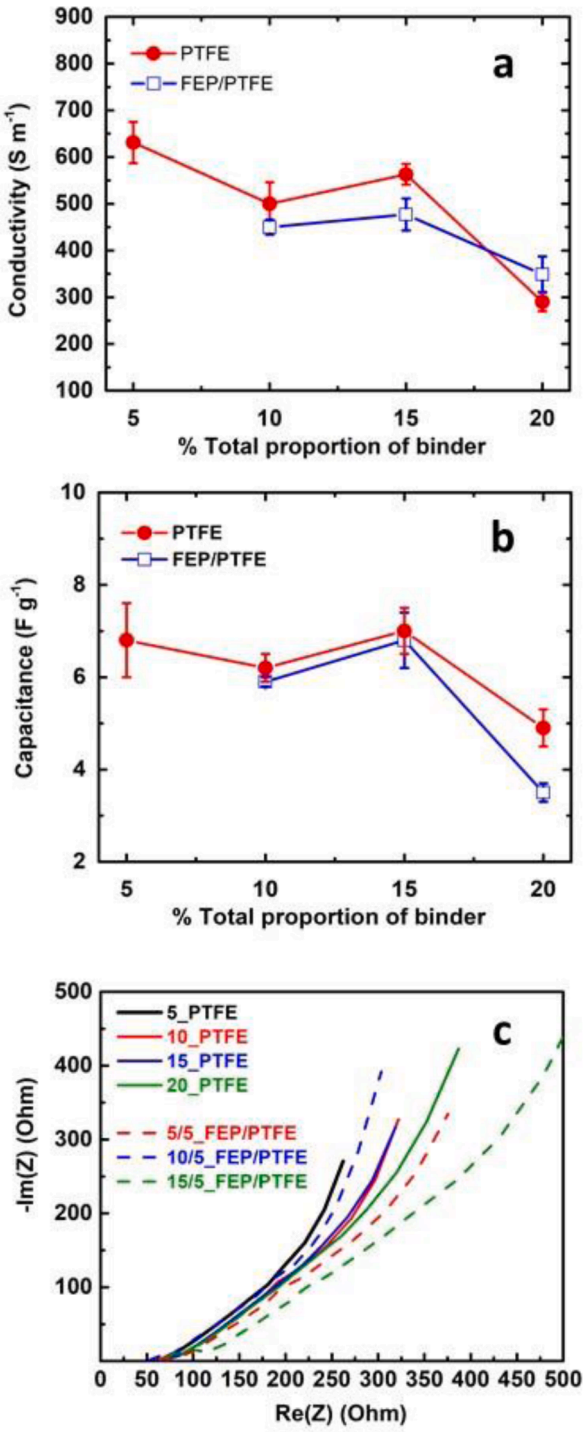

Fig. 5. (a) Electrical conductivity for both PTFE and FEP/PTFE series, measured by four-point probing. (b) Evolution of the capacitance with the total proportion of binder by integration of the cyclic voltammetry curves and the (c) Nyquist plots for both GNPs/PTFE and GNPs/FEP/PTFE series.

enhancement of the oxygen transport by the perfluorinated binder polymer. This phenomenon is clearly observed in Fig. 6d, where the preferential formation of sodium oxide at the 20_PTFE cathode/electrolyte interface was more evident. Thus, the bottom surface of 20_PTFE cathode is fully covered with sodium superoxide (green/yellow spots) while the sectional area is rich in carbon atoms (reds spots). The sodium oxide deposits in FEP/PTFE series also were displaced from the oxygen/cathode interface (5/5_FEP/PTFE, Fig. 6e) to the electrolyte/cathode interface (15/5_FEP/PTFE, Fig. 6g) by increasing the FEP proportion. The product displacement was not as evident as in the PTFE series since the oxide deposits were not so localized. Instead, small (nanometric) and highly distributed NaO_2 deposits (yellow and green spots) are dispersed withing the carbon-based cathode section. This can be attributed to the larger oxygen permeability of FEP compared with PTFE [29,30]. The dangling trifluoromethyl (-CF_3) group in FEP structure reduces the crystallinity by half compared to unbranched PTFE polymer [47], providing larger mechanical flexibility and cavities to fit the gas molecules [13,48]. The wettability of the cathodes was very similar in both PTFE to FEP/PTFE series (Fig. 5b and 5c) but, when analysing the cathodes on the oxygen pressurized atmosphere required to discharge a cell, the trend changed considerably (Fig. 6). We therefore hypothesize that FEP polymer might provide excessive oxygen transport to the cathodes (10^7 cm^2 sec^{-1}), to the detriment of electrolyte diffusion. In contrast, the diffusion coefficient of oxygen in PTFE polymer (10^{-6} cm^2 sec^{-1}) enables the modulation of the TPB sites within the air-cathode. It can be concluded that using perfluorinated polymers with too high oxygen affinity or polymer weight ratios above 15 wt.% causes the preferential deposition of the discharge products at the cathode/electrolyte interface. On the other hand, the strong interaction between molecular O_2 and C-F polarized bonds on perfluorinated polymers [13] could explain the formation of $Na_2O_2.2H_2O$ in those cathodes yielding larger ratios of PTFE polymer in Fig. 3b. The positive charge on carbon (induced by the electronegative fluor atom) will favour the O_2 adsorption and ORR kinetics at surface of the cathode, promoting the $2e^-$ mechanism ($O_2 \rightarrow O_2^{2-}$) over $1e^-$ mechanism ($O_2 \rightarrow O_2^-$) [49]. The more density of -CF_2- bonds in the cathode formulation (i.e., the larger polymer ratio) the most noticeable will be this phenomenon. Besides, the carbon atoms in -CF_3 group are more polarized than those in -CF_2- moiety, leading to larger amounts of peroxide-like side products in FEP cathodes (Fig. 3b), even at low polymer weight ratios. Even though a preferential (not exclusive) deposition of the discharge products in specific areas on the cathode section is confirmed as function of the polymer ratio and nature, the existence of discharge products in areas/interfaces different from the preferential one is also acknowledged. For instance, all the studied cathodes present discharge product particles at the oxygen/electrode interface, as observed in either cross-section (Fig. 6) or plain view (Fig. S3) SEM imaging. For low polymer concentrations (i.e., lower transport of oxygen from the gas reservoir to the cathode bulk) there is an excess of oxygen at the oxygen/cathode interface. Therefore, the growth of the particles is favoured in contrast to nucleation, leading to bigger NaO_2 cubes (micrometric). In contrast, for larger polymer ratios, oxygen gas molecules are mostly distributed towards the cathode bulk and/or at the cathode/electrolyte interface due to an enhanced oxygen transport. Thus, the limited concentration at the oxygen/cathode interface promotes the nucleation of numerous/small particles in the points where oxygen molecules are available and nano-sizes particles are therefore observed. The observed changes in the distribution and size of the discharge products affects significantly the discharge and cycling performance of the cathodes. The maximum discharge capacity is obtained for 10_PTFE cathode (4.5 mAh cm-2), which is the one presenting micron-sized deposits across the whole electrode area. Increasing the polymer weight ratio in 15_PTFE, causes the accumulation of the oxide at the cathode/electrolyte interface. This does not seem to be beneficial for discharge as both conductivity and wettability are similar for 10_PTFE and 15_PTFE but have completely different discharge behaviour. On the other hand, NaO2 deposits are distributed throughout the entire cathode area in 10_PTFE and 10/5_FEP/PTFE and their discharge capacity is similar. However, when cycling, the performance of the cells assembled with these cathodes was dramatically different. We hypothesized that the small size and high distribution of discharge products in 10/5_FEP/PTFE can be detrimental for charge, where nano-sizes particles may be difficult to dissolve [17].

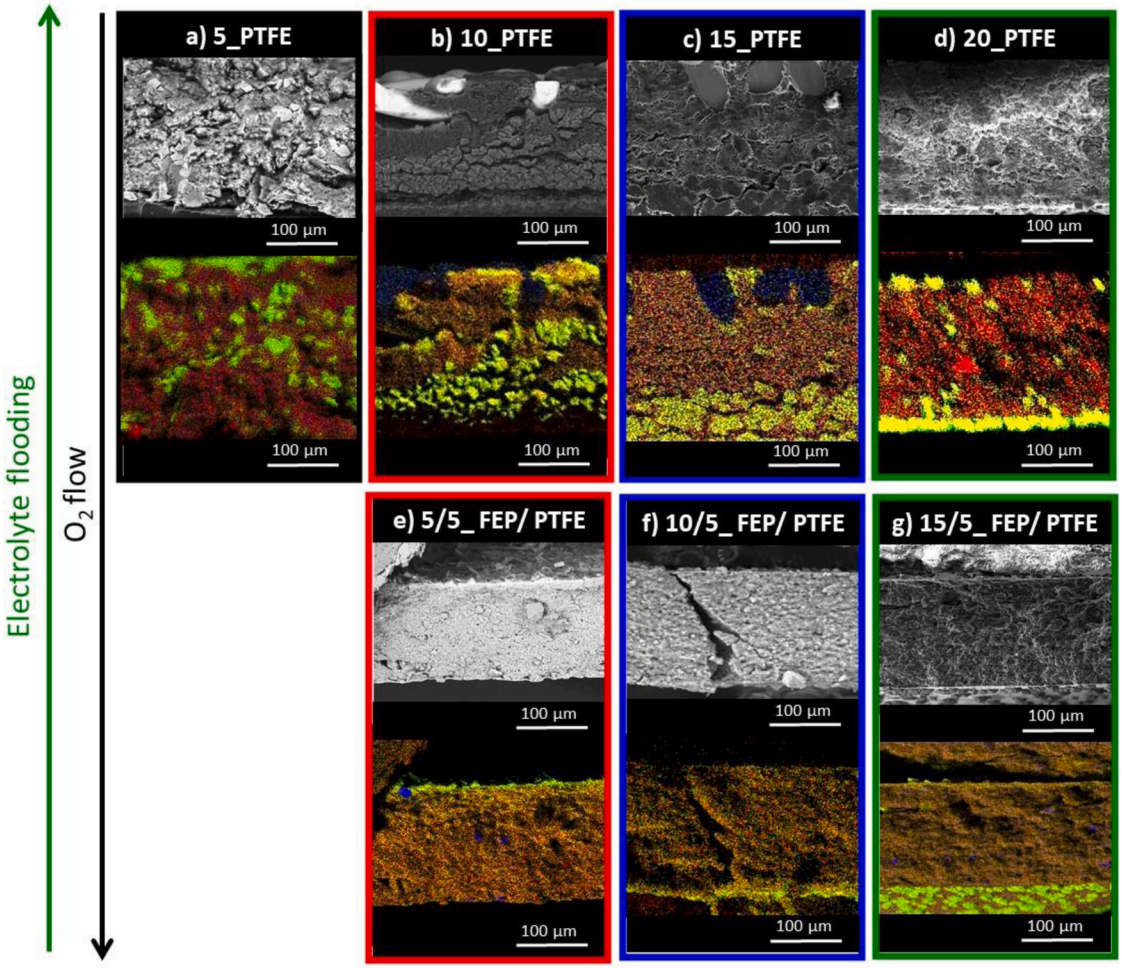

Fig. 6. Cross-sectional SEM imaging of the discharged electrodes and their respective EDX mapping for carbon (red), fluor (blue), sodium (yellow) and oxygen (green) atoms.

4. Conclusions

The combination of GNPs as active material and PTFE polymer as binder opens new opportunities to maximize the density of TPB points on Na-O_2 battery cathodes. This was not the case of FEP as the cathodes processed with this polymer presented poor mechanical properties and very poor cycling performance. The type of perfluorinated polymer did not affect the discharge capacity as much as cyclability, where the addition of FEP causes a dramatic decrease of both cycle life and overpotential. Besides processability, the electronic conductivity and the wettability of the GNP cathodes did not differ significantly from PTFE to FEP polymer. Hence, the much lower electrochemical performance of the latter was ascribed to an excessive O_2 transport. The utilization of relatively high polymer weight ratios, either PTFE or FEP, caused the displacement of the discharge products from the cathode bulk to the electrolyte/cathode interface, which resulted to be detrimental towards the battery performance. Hence, the increase of polarized C-F bonds in the cathode formulation will promote i) the preferential diffusion of oxygen gas over the liquid electrolyte, ii) the formation of $Na_2O_2{\cdot}2H_2O$ by 2 electron mechanism during ORR and iii) the passivation of the electrolyte/cathode interface by the oxide discharge products. The absence of highly polarized -CF_3 groups together with a linear structure provide a more moderate O_2 affinity to PTFE polymer, enabling the control of the gas diffusion properties on the electrode and a suitable distribution of the discharge products along the cathode section. The discharge capacity of the PTFE containing cathodes is maximized for polymer proportions around 10 wt.% (4.51 mAh cm^{-2} and 150 mV) and further decreases when using higher weight ratios. Proportions of binder over 10 wt.% provide limited discharge capacities and large discharge overpotentials. The cathode processed with 10 wt.% of PTFE polymer binder also present the best cycle life (142 cycles at 0.2 mA cm^{-2} and 0.5 mAh cm^{-2}), cycling overpotential (< 350 mV) and coulombic efficiency (100%) among all the studies samples. We can therefore conclude that the higher performance of this cathode was ascribed to an optimal balance between a moderate electrolyte wettability, electronic conductivity (500 S m^{-1}) and oxygen diffusion (~10^{-6} cm^2 sec^{-1}).

CRediT authorship contribution statement

M. Enterría: Conceptualization, Methodology, Writing – original draft, Formal analysis. **A. Letona-Elizburu:** Validation, Formal analysis, Investigation, Data curation, Writing – review & editing. **L. Medinilla:** Validation, Investigation, Writing – review & editing. **M. Echeverría:** Methodology, Investigation, Writing – review & editing. **N. Ortiz-Vitoriano:** Conceptualization, Methodology, Resources, Writing – review & editing, Supervision, Funding acquisition.

Declaration of Competing Interest

None.

Data Availability

Data will be made available on request.

Acknowledgments

This work was funded by the European Union (Graphene Flagship-Core 3, Grant No. 881603) and the R&D&I project PID2020–117626RA-I00, funded by MCIN/AEI/10.13039/501100011033. N. Ortiz-Vitoriano thanks Ramon y Cajal grant (RYC-2020-030104-I) funded by MCIN/AEI/10.13039/501100011033 and by FSE invest in your future.

Supplementary materials

Supplementary material associated with this article can be found, in the online version, at doi:10.1016/j.electacta.2022.141375.

References

[1] M. Enterría, M. Reynaud, J.I. Paredes, L. Medinilla, R. Younesi, N. Ortiz-Vitoriano, Driving the sodium-oxygen battery chemistry towards the efficient formation of discharge products: the importance of sodium superoxide quantification, J. Energy Chem. 68 (2022) 709–720, https://doi.org/10.1016/j.jechem.2021.12.014.

[2] R. Ebrahim, M. Yeleuov, A. Issova, S. Tokmoldin, A. Ignatiev, Triple-phase boundary and power density enhancement in thin solid oxide fuel cells by controlled etching of the nickel anode, Nanoscale Res. Lett. 9 (2014) 1–5, https://doi.org/10.1186/1556-276X-9-286.

[3] D. Schmitz, R. Anlauf, P. Rehrmann, Effect of air content on the oxygen diffusion coefficient of growing media, Am. J. Plant Sci. 04 (2013) 955–963, https://doi.org/10.4236/ajps.2013.45118.

[4] F. Mohazabrad, F. Wang, X. Li, Experimental studies of salt concentration in electrolyte on the performance of Li-O_2 batteries at various current densities, J. Electrochem. Soc. 163 (2016) A2623–A2627, https://doi.org/10.1149/2.0711613jes.

[5] F. Wang, X. Li, Effects of the electrode wettability on the deep discharge capacity of Li-O_2 batteries, ACS Omega 3 (2018) 6006–6012, https://doi.org/10.1021/acsomega.8b00808.

[6] S. Lee, J.S. Park, T.R. Lee, The wettability of fluoropolymer surfaces: influence of surface dipoles, Langmuir 24 (2008) 4817–4826, https://doi.org/10.1021/la700902h.

[7] J.K. Papp, J.D. Forster, C.M. Burke, H.W. Kim, A.C. Luntz, R.M. Shelby, J.J. Urban, B.D. McCloskey, Poly(vinylidene fluoride) (PVDF) binder degradation in Li-O2 batteries: a consideration for the characterization of lithium superoxide, J. Phys. Chem. Lett. 8 (2017) 1169–1174, https://doi.org/10.1021/acs.jpclett.7b00040.

[8] Q. Sun, X. Lin, H. Yadegari, W. Xiao, Y. Zhao, K.R. Adair, R. Li, X. Sun, Aligning the binder effect on sodium-air batteries, J. Mater. Chem. A 6 (2018) 1473–1484, https://doi.org/10.1039/c7ta09028e.

[9] T.A. Ha, H. Li, X. Wang, L.A. O'Dell, M. Forsyth, C. Pozo-Gonzalo, P.C. Howlett, Functional binders based on polymeric ionic liquids for sodium oxygen batteries using ionic liquid electrolytes, ACS Appl. Energy Mater. 4 (2021) 434–444, https://doi.org/10.1021/acsaem.0c02352.

[10] E. Nasybulin, W. Xu, M.H. Engelhard, Z. Nie, X.S. Li, J.G. Zhang, Stability of polymer binders in Li-O_2 batteries, J. Power Sources 243 (2013) 899–907, https://doi.org/10.1016/j.jpowsour.2013.06.097.

[11] K.C. Lowe, Perfluorinated blood substitutes and artificial oxygen carriers, Blood Rev. 13 (1999) 171–184, https://doi.org/10.1054/blre.1999.0113.

[12] J.G. Riess, Reassessment of criteria for the selection of perfluorochemicals for second-generation blood substitutes: analysis of structure/property relationships, Artif. Organs 8 (1984) 44–56, https://doi.org/10.1111/j.1525-1594.1984.tb04243.x.

[13] A.M.A. Dias, C.M.B. Gonçalves, J.L. Legido, J.A.P. Coutinho, I.M. Marrucho, Solubility of oxygen in substituted perfluorocarbons, Fluid Phase Equilib. 238 (2005) 7–12, https://doi.org/10.1016/j.fluid.2005.09.011.

[14] Y. Li, J. Wang, X. Li, D. Geng, R. Li, X. Sun, Superior energy capacity of graphene nanosheets for a nonaqueous lithium-oxygen battery, Chem. Commun. 47 (2011) 9438–9440, https://doi.org/10.1039/c1cc13464g.

[15] C.L. Bender, P. Hartmann, M. Vračar, P. Adelhelm, J. Janek, On-the thermodynamics, the role of the carbon cathode, and the cycle life of the sodium superoxide (NaO_2) battery, Adv. Energy Mater. 4 (2014), 1301863, https://doi.org/10.1002/aenm.201301863.

[16] S. Liu, S.S. Liu, J.Y. Luo, Carbon-based cathodes for sodium-air batteries, New Carbon Mater. 31 (2016) 264–270, https://doi.org/10.1016/S1872-5805(16)60012-4.

[17] Z. Jian, Y. Chen, F. Li, T. Zhang, C. Liu, H. Zhou, High capacity Na-O_2 batteries with carbon nanotube paper as binder-free air cathode, J. Power Sources 251 (2014) 466–469, https://doi.org/10.1016/j.jpowsour.2013.11.091.

[18] T.A. Ha, C. Pozo-Gonzalo, K. Nairn, D.R. MacFarlane, M. Forsyth, P.C. Howlett, An investigation of commercial carbon air cathode structure in ionic liquid based sodium oxygen batteries, Sci. Rep. 10 (2020) 1–10, https://doi.org/10.1038/s41598-020-63473-y.

[19] M. Enterría, C. Botas, J.L. Gómez-Urbano, B. Acebedo, J.M. López Del Amo, D. Carriazo, T. Rojo, N. Ortiz-Vitoriano, Pathways towards high performance Na-O_2 batteries: tailoring graphene aerogel cathode porosity & nanostructure, J. Mater. Chem. A 6 (2018) 20778–20787, https://doi.org/10.1039/c8ta07273f.

[20] X. Lin, J. Wang, X. Gao, S. Wang, Q. Sun, J. Luo, C. Zhao, Y. Zhao, X. Yang, C. Wang, R. Li, X. Sun, 3D printing of free-standing "O_2 breathable" air electrodes for high-capacity and long-life Na–O_2 batteries, Chem. Mater. 32 (2020) 3018–3027, https://doi.org/10.1021/acs.chemmater.9b05360.

[21] D.Y. Kim, M. Kim, D.W. Kim, J. Suk, J.J. Park, O.O. Park, Y. Kang, Graphene paper with controlled pore structure for high-performance cathodes in Li-O2 batteries, Carbon 100 (2016) 265–272, https://doi.org/10.1016/j.carbon.2016.01.013. N Y.

[22] W. Zhou, H. Zhang, H. Nie, Y. Ma, Y. Zhang, H. Zhang, Hierarchical micron-sized mesoporous/macroporous graphene with well-tuned surface oxygen chemistry for high capacity and cycling stability Li-O_2 battery, ACS Appl. Mater. Interfaces 7 (2015) 3389–3397, https://doi.org/10.1021/am508513m.

[23] X. Zhong, B. Papandrea, Y. Xu, Z. Lin, H. Zhang, Y. Liu, Y. Huang, X. Duan, Three-dimensional graphene membrane cathode for high energy density rechargeable lithium-air batteries in ambient conditions, Nano Res. 10 (2017) 472–482, https://doi.org/10.1007/s12274-016-1306-4.

[24] Ş. Özcan, T. Cetinkaya, M. Tokur, H. Algül, M.O. Guler, H. Akbulut, Synthesis of flexible pure graphene papers and utilization as free standing cathodes for lithium-air batteries, Int. J. Hydrog. Energy 41 (2016) 9796–9802, https://doi.org/10.1016/j.ijhydene.2016.02.044.

[25] J.L. Gómez Urbano, M. Enterría, I. Monterrubio, I. Ruiz de Larramendi, D. Carriazo, N.O. Vitoriano, T. Rojo, An overview of engineered graphene-based cathodes: boosting oxygen reduction and evolution reactions in lithium and sodium oxygen batteries, ChemSusChem 13 (2019) 1203–1225, https://doi.org/10.1002/cssc.201902972.

[26] K.A. Novčić, A.S. Dobrota, M. Petković, B. Johansson, N.V. Skorodumova, S. V. Mentus, I.A. Pašti, Theoretical analysis of doped graphene as cathode catalyst in Li-O_2 and Na-O_2 batteries – the impact of the computational scheme, Electrochim. Acta 354 (2020), 136735, https://doi.org/10.1016/j.electacta.2020.136735.

[27] W. Liu, Q. Sun, Y. Yang, J.Y. Xie, Z.W. Fu, An enhanced electrochemical performance of a sodium–air battery with graphene nanosheets as air electrode catalysts, Chem. Commun. 49 (2013) 1951–1953, https://doi.org/10.1039/c3cc00085k.

[28] Y. Li, J. Wang, X. Li, D. Geng, R. Li, X. Sun, Superior energy capacity of graphene nanosheets for a nonaqueous lithium-oxygen battery[CE: *duplicate reference of* 14], Chem. Commun. 47 (2011) 9438–9440, https://doi.org/10.1039/c1cc13464g.

[29] N.T.S. Evans, T.H. Quinton, Permeability and diffusion coefficient of oxygen in membranes for oxygen electrodes, Respir. Physiol. 35 (1978) 89–99.

[30] W.J. Koros, J. Wang, R.M. Felder, Oxygen permeation through FEP teflon and kapton polyimide, J. Appl. Polym. Sci. 26 (1981) 2805–2809, https://doi.org/10.1002/app.1981.070260832.

[31] M. Thommes, K. Kaneko, A.V. Neimark, J.P. Olivier, F. Rodriguez-Reinoso, J. Rouquerol, K.S.W. Sing, Physisorption of gases, with special reference to the evaluation of surface area and pore size distribution (IUPAC Technical Report), Pure Appl. Chem. 87 (2015) 1051–1069, https://doi.org/10.1515/pac-2014-1117.

[32] A. González, E. Goikolea, J.A. Barrena, R. Mysyk, Review on supercapacitors: technologies and materials, Renew, Sustain. Energy Rev. 58 (2016) 1189–1206, https://doi.org/10.1016/j.rser.2015.12.249.

[33] N. Rey-Raap, E.G. Calvo, J.M. Bermúdez, I. Cameán, A.B. García, J.A. Menéndez, A. Arenillas, An electrical conductivity translator for carbons, Meas. J. Int. Meas. Confed. 56 (2014) 215–218, https://doi.org/10.1016/j.measurement.2014.07.003.

[34] A. Sayah, F. Habelhames, A. Bahloul, B. Nessark, Y. Bonnassieux, D. Tendelier, M. El Jouad, Electrochemical synthesis of polyaniline-exfoliated graphene composite films and their capacitance properties, J. Electroanal. Chem. 818 (2018) 26–34, https://doi.org/10.1016/j.jelechem.2018.04.016.

[35] F.T. Johra, J.W. Lee, W.G. Jung, Facile and safe graphene preparation on solution based platform, J. Ind. Eng. Chem. 20 (2014) 2883–2887, https://doi.org/10.1016/j.jiec.2013.11.022.

[36] R. Rozada, J.I. Paredes, S. Villar-Rodil, A. Martínez-Alonso, J.M.D. Tascón, Towards full repair of defects in reduced graphene oxide films by two-step graphitization, Nano Res. 6 (2013) 216–233, https://doi.org/10.1007/s12274-013-0298-6.

[37] N. Ortiz-Vitoriano, T.P. Batcho, D.G. Kwabi, B. Han, N. Pour, K.P.C. Yao, C. V. Thompson, Y. Shao-Horn, Rate-dependent nucleation and growth of NaO_2 in Na-O_2 batteries, J. Phys. Chem. Lett. 6 (2015) 2636–2643, https://doi.org/10.1021/acs.jpclett.5b00919.

[38] N. Zhao, C. Li, X. Guo, Long-life Na–O2 batteries with high energy efficiency enabled by electrochemically splitting NaO_2 at a low overpotential, Phys. Chem. Chem. Phys. 16 (2014) 15646–15652, https://doi.org/10.1039/C4CP01961J.

[39] R. Pinedo, D.A. Weber, B. Bergner, D. Schröder, P. Adelhelm, J. Janek, Insights into the chemical nature and formation mechanisms of discharge products in Na-O_2 batteries by means of operando X-ray diffraction, J. Phys. Chem. C 120 (2016) 8472–8481, https://doi.org/10.1021/acs.jpcc.6b00903.

[40] X. Bi, R. Wang, L. Ma, D. Zhang, K. Amine, J. Lu, Sodium peroxide dihydrate or sodium superoxide: the importance of the cell configuration for sodium–oxygen batteries, Small Methods 1 (2017), 1700102, https://doi.org/10.1002/smtd.201700102.

[41] M. Enterría, J.L. Gómez-Urbano, J.M. Munuera, S. Villar-Rodil, D. Carriazo, J. I. Paredes, N. Ortiz-Vitoriano, Boosting the performance of graphene cathodes in Na–O_2 batteries by exploiting the multifunctional character of small biomolecules, Small 17 (2021), 2005034, https://doi.org/10.1002/smll.202005034.

[42] J.M. Munuera, J.I. Paredes, M. Enterría, S. Villar-Rodil, A.G. Kelly, Y. Nalawade, J. N. Coleman, T. Rojo, N. Ortiz-Vitoriano, A. Martínez-Alonso, J.M.D. Tascón, High performance Na-O_2 batteries and printed microsupercapacitors based on water-processable, biomolecule-assisted anodic graphene, ACS Appl. Mater. Interfaces 12 (2020) 494–506, https://doi.org/10.1021/acsami.9b15509.

[43] J.H. Kang, W.J. Kwak, D. Aurbach, Y.K. Sun, Sodium oxygen batteries: one step further with catalysis by ruthenium nanoparticles, J. Mater. Chem. A 5 (2017) 20678–20686, https://doi.org/10.1039/c7ta06584a.
[44] N. Li, Y. Yin, F. Meng, Q. Zhang, J. Yan, Q. Jiang, Enabling pyrochlore-type oxides as highly efficient electrocatalysts for high-capacity and stable Na-O_2 batteries: the synergy of electronic structure and morphology, ACS Catal. 7 (2017) 7688–7694, https://doi.org/10.1021/acscatal.7b02074.
[45] Z. Zheng, J. Jiang, H. Guo, C. Li, K. Konstantinov, Q. Gu, J. Wang, Tuning NaO_2 formation and decomposition routes with nitrogen-doped nanofibers for low overpotential Na-O_2 batteries, Nano Energy 81 (2021), 105529, https://doi.org/10.1016/j.nanoen.2020.105529.
[46] H. Li, T.A. Ha, N. Ortiz-Vitoriano, X. Wang, J. Fang, P.C. Howlett, C. Pozo-Gonzalo, Tunable multi-doped carbon nanofiber air cathodes based on a poly(ionic liquid) for sodium oxygen batteries with diglyme/ionic liquid-based hybrid electrolytes, J. Mater. Chem. A 10 (2022) 11742–11754, https://doi.org/10.1039/d2ta01586b.
[47] Elsevier, Introduction to Fluoropolymers, Elsevier, 2013, pp. 63–89, https://doi.org/10.1016/b978-1-4557-7442-5.00006-1, in: Introd. to Fluoropolymers.
[48] C. Xia, S. Back, S. Ringe, K. Jiang, F. Chen, X. Sun, S. Siahrostami, K. Chan, H. Wang, Confined local oxygen gas promotes electrochemical water oxidation to hydrogen peroxide, Nat. Catal. 3 (2020) 125–134, https://doi.org/10.1038/s41929-019-0402-8.
[49] C.L. Bender, D. Schröder, R. Pinedo, P. Adelhelm, J. Janek, One- or two-electron transfer? The ambiguous nature of the discharge products in sodium-oxygen batteries, angew, Chem. Int. Ed. 55 (2016) 4640–4649, https://doi.org/10.1002/anie.201510856.